# Discovery of Double-ring Structure in the Supernova Remnant N103B: Evidence for Bipolar Winds from a Type Ia Supernova Progenitor

Hiroya Yamaguchi[1,2] , Fabio Acero[3] , Chuan-Jui Li[4] , and You-Hua Chu[4]

[1] Institute of Space and Astronautical Science, JAXA, 3-1-1 Yoshinodai, Sagamihara, Kanagawa 229–8510, Japan; yamaguchi@astro.isas.jaxa.jp
[2] Department of Physics, The University of Tokyo, Hongo, Bunkyo, Tokyo, 113-0033, Japan
[3] Département d'Astrophysique-AIM, CEA/DRF/IRFU, CNRS/INSU, Université Paris-Saclay, Université de Paris, Gif-sur-Yvette, France
[4] Institute of Astronomy and Astrophysics, Academia Sinica, No.1, Sec. 4, Roosevelt Road, Taipei 10617, Taiwan

## Abstract

The geometric structure of supernova remnants (SNR) provides a clue to unveiling the pre-explosion evolution of their progenitors. Here we present an X-ray study of N103B (0509–68.7), a Type Ia SNR in the Large Magellanic Cloud, that is known to be interacting with dense circumstellar matter (CSM). Applying our novel method for feature extraction to deep Chandra observations, we have successfully resolved the CSM, Fe-rich ejecta, and intermediate-mass element (IME) ejecta components, and revealed each of their spatial distributions. Remarkably, the IME ejecta component exhibits a double-ring structure, implying that the SNR expands into an hourglass-shape cavity and thus forms bipolar bubbles of the ejecta. This interpretation is supported by more quantitative spectroscopy that reveals a clear bimodality in the distribution of the ionization state of the IME ejecta. These observational results can be naturally explained if the progenitor binary system had formed a dense CSM torus on the orbital plane prior to the explosion, providing further evidence that the SNR N103B originates from a single-degenerate progenitor.

## 1. Introduction

Type Ia supernovae (SNe Ia) are utilized as distance indicators to constrain the cosmological parameters and the nature of the dark energy (e.g., Suzuki et al. 2012, and references therein). Although it is generally accepted that SNe Ia originate from a thermonuclear explosion of a carbon–oxygen white dwarf (WD) in a binary system, their evolution channel is still under debate. One hypothesis is that the thermonuclear explosion is caused by a merger of two WDs, which is called the double-degenerate (DD) scenario (e.g., Iben & Tutukov 1984; Webbink 1984) and often associated with an explosion of a sub-Chandrasekhar-mass (sub-$M_{Ch}$) WD (e.g., Fink et al. 2010; Shen et al. 2018). Another hypothesis is the so-called single-degenerate (SD) scenario, where a WD accretes hydrogen-rich matter from a nondegenerate companion and explodes when the WD mass approaches $M_{Ch}$ (e.g., Whelan & Iben 1973; Nomoto 1982). Recent observations tend to support the DD scenario, based on the lack of a surviving companion in Type Ia supernova remnants (SNRs Ia; e.g., Schaefer & Pagnotta 2012; Kerzendorf et al. 2013, 2018; Ruiz-Lapuente et al. 2018) or the lack of the signature of interaction between SN Ia ejecta and a nondegenerate companion in either early phase lightcurve (e.g., Brown et al. 2012; Olling et al. 2015) or nebula-phase spectra (e.g., Shappee et al. 2013; Lundqvist et al. 2015; Sand et al. 2018; Dimitriadis et al. 2019; Tucker et al. 2019). Moreover, the delay time distribution of SNe Ia favors the DD channel as the major contributor to these events (e.g., Totani et al. 2008; Maoz et al. 2010). However, contributions of the near-$M_{Ch}$ progenitors are also necessary from the perspective of the cosmic chemical evolution, suggesting that both SD and DD channels may end up as SNe Ia (e.g., Seitenzahl et al. 2013; Hitomi Collaboration et al. 2017; Kobayashi et al. 2020). It is, therefore, crucial to identify the exact relationship between the different evolution channels

and different observational characteristics of SNe Ia (and their remnants), which in turn enables even more robust distance measurements in cosmology.

An important prediction of the SD scenarios is the presence of mass outflow from the binary system during the pre-SN evolution (e.g., Hachisu et al. 1996). Therefore, detection of circumstellar matter (CSM) from SNe Ia is naturally interpreted as evidence of their SD progenitor origin (e.g., Hamuy et al. 2003; Simon et al. 2009; Sternberg et al. 2011; Silverman et al. 2013). The presence of CSM is confirmed also in a handful of young SNRs Ia, which offer a unique opportunity to investigate their CSM's spatial distribution, providing the key for understanding how their progenitor systems have evolved exactly. One of such objects is Kepler's SNR, the relic of SN 1604 (Blair et al. 1991; Gerardy & Fesen 2001). In this SNR, a significant amount of the CSM is located at the northern rim and the central region, with little evidence for dense materials in the south (Blair et al. 2007; Reynolds et al. 2007; Williams et al. 2012). The north–south asymmetry of the CSM is suggested to be formed by the wind activity of the progenitor system moving toward the north (Borkowski et al. 1992; Chiotellis et al. 2012). The other CSM concentration found near the projected SNR center is claimed as evidence for a disk distribution of the CSM around the pre-explosion progenitor system (Burkey et al. 2013).

The SNR N103B (0509–68.7), located near the edge of the central bar of the Large Magellanic Cloud (LMC), is another SNR Ia that is known to be interacting with a dense CSM (e.g., Williams et al. 2014). The age of the SNR is estimated to be less than 1000 years from the light echo observations and shock velocity measurement (Rest et al. 2005; Ghavamian et al. 2017; Williams et al. 2018). Because of its proximity to the ionized superbubble around the NGC 1850 cluster, N103B was initially identified as a core-collapse SNR (Chu & Kennicutt 1988). This interpretation was supported by X-ray observations using

the XMM-Newton Reflection Grating Spectrometer (RGS), based on the detection of strong O emission (van der Heyden et al. 2002). However, a high-resolution imaging study and spatially resolved spectroscopy with Chandra revealed that the O emission likely originated from the CSM rather than the SN ejecta (Lewis et al. 2003). The authors also argued that the estimated ejecta mass of Si and Fe were consistent with predictions of typical SN Ia products, confirming the previous spectroscopic results of ASCA observations (Hughes et al. 1995).

Similar to Kepler's SNR, N103B exhibits a highly asymmetric morphology in various wavelengths, with the brightness enhanced toward the west (e.g., Williams et al. 1999; Lewis et al. 2003; Alsaberi et al. 2019). Using high-resolution optical images from the Hubble Space Telescope (HST), Li et al. (2017) spatially resolved the complex radiative clumps that are located inside an Balmer-dominated filamentary shell. The density of the clumps is generally higher than $100 \, \mathrm{cm}^{-3}$ and even reaches $\sim 5000 \, \mathrm{cm}^{-3}$ in the densest regions, providing clear evidence of their CSM origin. The H$\alpha$ emission from these clumps is significantly redshifted, suggesting the one-sided distribution of the CSM (Li et al. 2017; Ghavamian et al. 2017). This asymmetry is thought to have originated from a proper motion of the progenitor binary system toward the west. It is notable, however, that radio observations with the Australia Telescope Compact Array (ATCA) and Atacama Large Millimeter/submillimeter Array (ALMA) discovered a giant molecular cloud toward the southeast of the SNR (Sano et al. 2018). The cloud shows an expanding gas motion with its spatial extent along the SNR rim, which strongly suggests the SNR-cloud interaction indeed taking place there. The average H$_2$ density in the interacting region is estimated to be $\sim 1500 \, \mathrm{cm}^{-3}$, even higher than the typical atomic hydrogen density in the west. This fact suggests that the absence of the H$\alpha$ emission in the eastern side of the SNR is not due to the low ambient density, but is due to the chemical composition dominated by the molecular hydrogen. The elemental abundance of the CSM is consistent with the local interstellar medium (ISM) of the LMC (Blair et al. 2020), implying that the companion of N103B must have been a main-sequence star, rather than more evolved ones, such as an asymptotic giant branch star.[5] To summarize, N103B is an SNR Ia likely originating from a relatively young SD progenitor system that has experienced substantial mass loss prior to the explosion, and is now interacting with the CSM with a spherically asymmetric distribution. These characteristics make this object an ideal laboratory for probing into the nature of SD progenitors in general.

This paper presents an X-ray study of N103B based on the latest deep Chandra observations. Although the observations were conducted primarily for an expansion velocity measurement (Williams et al. 2018), the data are remarkably suitable for spatially resolved spectroscopy as well. Our immediate aim is to determine the geometry of the SN ejecta and CSM, independently from the previous multiwavelength studies, in order to constrain the pre-explosion activity of its progenitor. To achieve this goal, we apply the new feature extraction technique established by Picquenot et al. (2019), and perform detailed spectral analysis. The uncertainties quoted in the text

and table and the error bars given in the figures represent a $1\sigma$ confidence level, unless otherwise stated.

## 2. Analysis and Results

### 2.1. Observations and Data Reprocess

The SNR N103B was observed by Chandra in the Spring of 2017 (between March 20 and June 1) using the ACIS-S3 chip primarily for the expansion velocity measurement (Williams et al. 2018). The resulting data consist of 12 separate observations with different satellite roll angles. Since the calibration database (CALDB) for the ACIS instrument has been updated after the observations, we reprocess the data using CIAO version 4.12.1 and the latest CALDB (v.4.9.2.1) for the present work. After the standard data screening, we obtain a total effective exposure of 393 ks.

### 2.2. Component Extraction: Methods

We conduct the feature extraction based on the Generalized Morphological Components Analysis (GMCA) described in Picquenot et al. (2019)[6] to disentangle different physical components present in the data and to identify the extraction regions of interest. Imaging spectroscopy instruments, such as the Chandra ACIS, provide "three-dimensional" data cubes of the photon positions and energy $(x, y, E)$. The GMCA is a source separation method that looks for clusters of voxels in the data cube with similar spectral signatures. This method assumes that different physical components (e.g., shocked ejecta and nonthermal emission) have different morphologies in addition to different spectral signatures, and fully exploits the multidimensional aspect of the X-ray data. It is a blind approach and has no prior instrumental or physical information. Therefore, the components do not come with a label, and physical interpretation is to be made by users based on the decomposed spectra and images. Inputs to the algorithm are the data cube and the user-defined number $N$ of components to retrieve. The output is a set of $N$ images and spectra with different morphological and spectral signatures.

To build the data cube needed for our feature extraction applied to N103B, we merge the event lists from the 12 separate observations. The spatial and spectral binning are optimized to be $0.''75$ and $87.6 \, \mathrm{eV}$ (corresponding to six spectral channels of the ACIS), respectively, to achieve an ideal balance between the statistics in each voxel and retainment of enough spatial and spectral information. The number of components is fixed to three, obtaining the set of decomposed images and spectra given in Figure 1. An addition of the fourth component results in overfitting of the data; two of the four components show similar images and spectra. Therefore, we conclude that the optimal number for our data is three.

### 2.3. Component Extraction: Results

The first panel (Figure 1(a)) shows the spectrum of each retrieved component. Component 1 (red) is characterized by the strong O K emission below 0.7 keV, suggesting a CSM origin of this components. Component 2 (green) consists mainly of the Fe L-shell ($\sim 1$ keV) and K-shell ($\sim 6.5$ keV) emission, and thus can be associated with the Fe-rich ejecta originating from the nuclear statistical equilibrium achieved during the

---

[5] In contrast, two surviving companion candidates found in other SNRs Ia in the LMC are both located in the red giant branch (Li et al. 2019).

[6] This technique was first introduced by Bobin et al. (2016) for the cosmic microwave background (CMB) reconstruction.
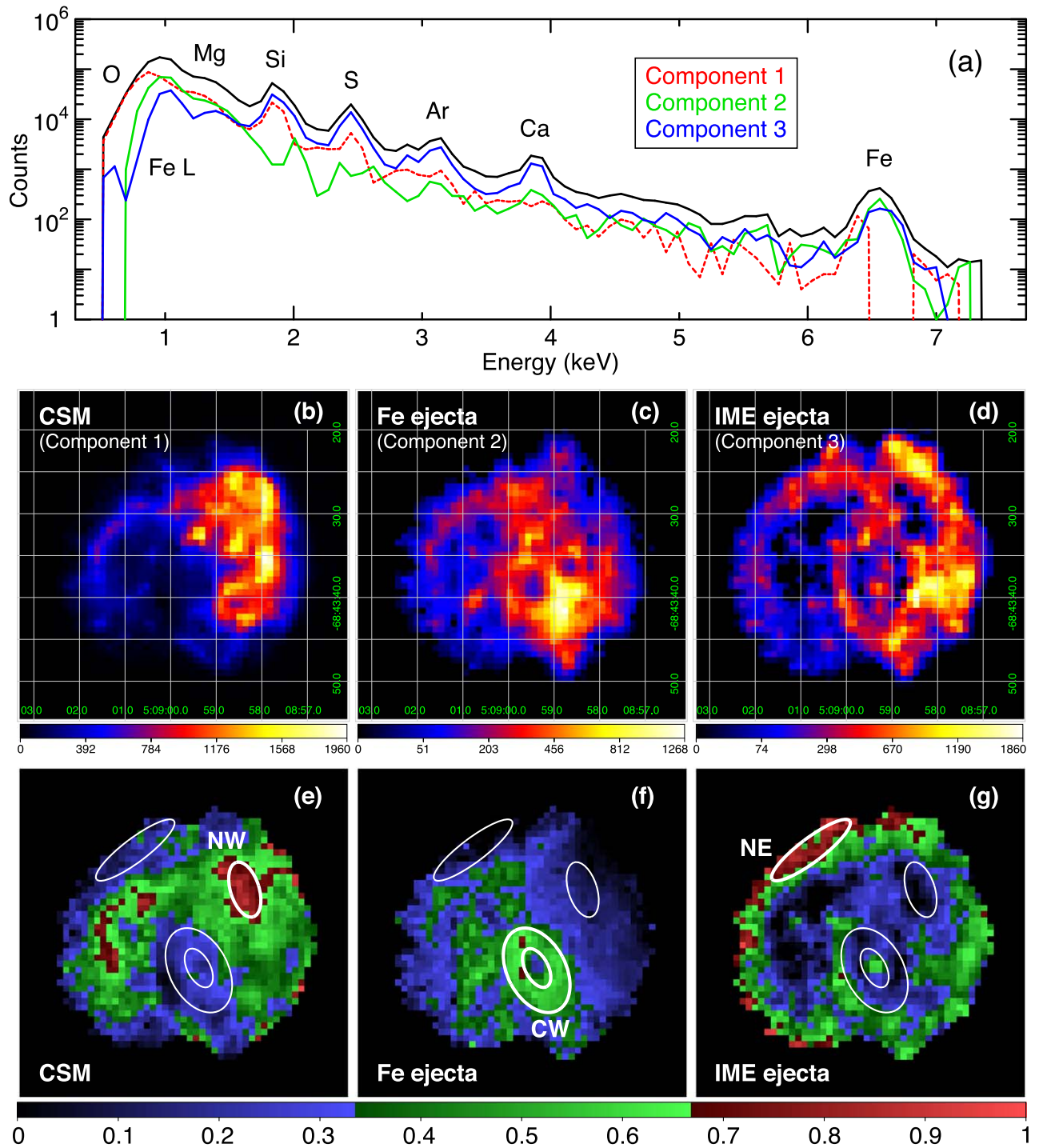
**Figure 1.** Results of the GMCA applied to the SNR N103B. Top: retrieved spectra of the three components. Middle: spatial distribution of the retrieved components. The pixel values correspond to the photon counts normalized by the count in the single brightest pixel. Panel (b) is given in the linear scale, whereas panels (c) and (d) are in the square root scale. Bottom: fraction of each component (see the text) given in the linear scale. The ellipses indicate where the spectra shown in Figures 4 and 7 are extracted.

progenitor's explosion. The retrieved spectrum of Component 3 (blue) dominates the line flux of the intermediate-mass elements (IME: Si, S, Ar, and Ca) and reproduces also a part of the Fe emission detected in the spectrum of the entire SNR. This characteristic is consistent with the emission from incomplete Si burning products typically observed in other SNRs Ia (e.g., Tycho and Kepler). Given the results, we hereafter call Components 1, 2, and 3 "CSM," "Fe ejecta," and "IME ejecta," respectively. This identification will be verified

later with detailed analysis of the X-ray spectra as well as comparison with optical observations.

Figures 1(b), (c), and (d) present the spatial distribution of the CSM, Fe ejecta, and IME ejecta, respectively. The pixel value indicates the photon counts of each component. The CSM image exhibits several clumpy features in the west, which spatially coincide with the optical nebula knots (Ghavamian et al. 2017; Li et al. 2017, see also Section 3). The emission from the Fe ejecta is strongest in the southwest, consistent with
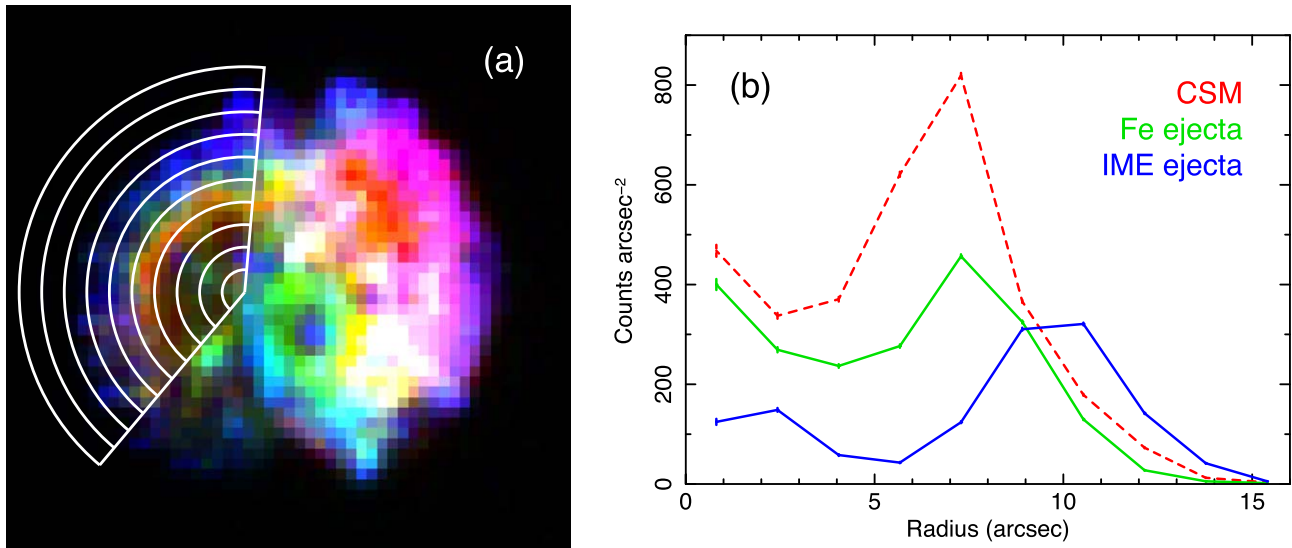
**Figure 2.** (a) Three-color image of the SNR N103B. Red (dashed), green, and blue are the CSM, Fe ejecta, and IME ejecta components, respectively. (b) Radial profiles extracted from the sectors shown in panel (a), which confirms that the IME ejecta component peaks at a larger radius than the others.
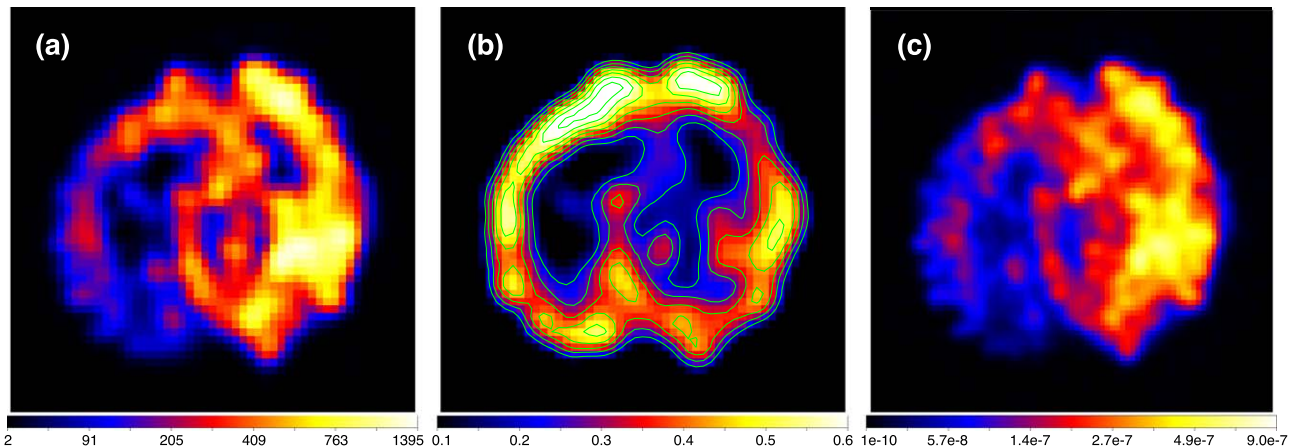


**Figure 3.** Spatial distribution of the IME ejecta component. Panels (a) and (b) are essentially the same of Figures 1(d) and (g), but smoothed to highlight the double-ring structure. Panel (c) is a simple flux image of the Si K band (1.80–2.05 keV) in units of photon cm$^{-2}$ s$^{-1}$.

the previous XMM-Newton observation (van der Heyden et al. 2002) but is revealed more clearly with a higher spatial resolution. The IME ejecta are also prominent in the west, but its morphology is distinctly different from those of the other components. There are several remarkable features revealed in this image. First, not only in the bright western rim but also in the fainter east, the spatial extent of this component is larger than those of the other components, which is also confirmed in the radial profiles given in Figure 2. Second, its morphology does not seem to be a single shell but looks apparently a double-ring structure, like "pretzel," consisting of two elliptical shells crossing each other around the geometrical center of the SNR.

The third row of Figure 1 shows the fraction of each component, defined as $f_i = N_i/(N_1 + N_2 + N_3)$, where $N_i$ is the photon counts of Component $i$ normalized by the maximum pixel count obtained for each component. The enhancement of the IME ejecta at the SNR rim is confirmed even more clearly in Figure 1(g). It should be noted that a similar radial structure was revealed in the equivalent width maps of the He-like Si and S emission by the previous Chandra study (Lewis et al. 2003), where little azimuthal dependence in the equivalent width was

found as well. Our analysis confirms the same trend with an independent approach applied to the much longer exposure data.

The double-ring structure of the IME ejecta component is more clearly seen in Figures 3(a) and (b), which are essentially the same as Figures 1(d) and (g), respectively, but are smoothed to emphasize the image contrast. We also show in Figure 3(c) a narrowband flux image of the Si K band (1.80–2.05 keV) generated using the flux_obs script in the CIAO package. The double-ring shape already appears in this simply processed image, indicating that this intriguing structure is not an artifact owing to our new analysis methods.

### 2.4. Spectral Characteristics

We extract spectra from three representative regions, NW, CW, and NE in Figure 1, containing pixels with large $f_i$ values for each of the identified components. The background data are taken from the nearby source-free region and subtracted from the sources. The obtained spectra are compared in Figure 4. As expected, the spectrum of NW (red) exhibits an enhanced flux below ~0.7 keV, and that of CW (green) shows the strongest
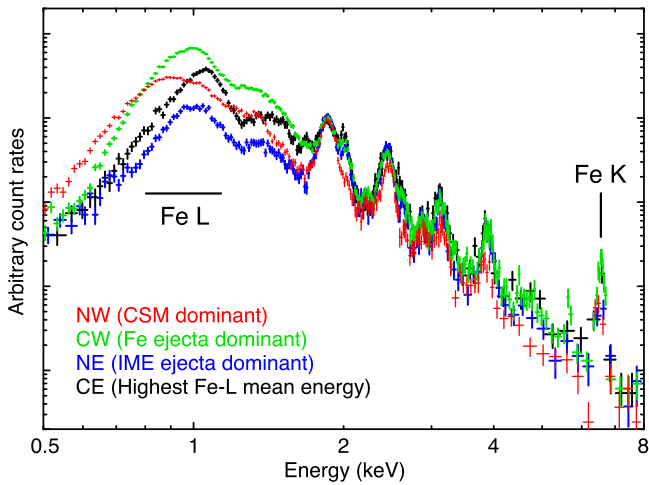
**Figure 4.** Comparison of the ACIS spectra extracted from the regions indicated in Figures 1 or 4: NW (red), CW (green), NE (blue), and CE (black).



**Figure 5.** Mean energy of the Fe L-shell emission in 0.8–1.2 keV. The contours are the same as those presented in Figure 3(b).



**Figure 6.** (a) Mean energy of the Si K-shell emission in 1.80–2.05 keV. The contours are the same as those presented in Figure 3(b). (b) The 1.6–2.8-keV spectra extracted from the regions indicated in panel (a).

Fe emission (both L-shell and K-shell) with respect to the IME emission. The centroid energy of the Fe K emission in the CW spectrum is found to be ∼6.54 keV, consistent with the Suzaku measurement of the entire SNR's spectrum (Yamaguchi et al. 2014).

Also remarkable in Figure 4 is that the shape of the Fe L-shell blend around 1 keV is substantially different among the spectra, implying that the dominant charge states of Fe ions are different from region to region. To investigate this variety more comprehensively, we map the mean energy of the X-ray photons detected in the 0.8–1.2 keV band using the `mean_energy_map` script in CIAO. The result is shown as the color map in Figure 5, where the $f_3$ image (same as Figure 3(b)) is overplotted in contours. We find that the mean energy of the Fe L emission is well correlated with the $f_3$ value, suggesting that Fe ions in the IME component are generally more highly ionized. In contrast, the regions dominated by the CSM component have lower mean energies (i.e., lower charge state of Fe). Notably, the highest mean is found at the region labeled "CE" (blue dashed polygon) in Figure 5, which corresponds to the eastern side of the "west ring." The spectrum of this region is also shown in Figure 4 with the black data points, confirming the Fe L blend with a significantly high centroid.

Figure 4 also indicates considerable spatial variability in the Si Lyα/Heα ratio. We thus generate another mean energy map using the 1.80–2.05 keV photons in Figure 6(a). Interestingly, the mean energy distribution is clearly bimodal; the interior of the east ring (hereafter East bubble) globally has the high mean energies, and that of the west ring (West bubble) the lower means. The Si K band spectra of the East and West bubbles are shown in Figure 6(b). The Lyα/Heα flux ratios are indeed largely different between the two regions, indicating that the IME ejecta are more highly ionized in the East bubble than in the West one.

### 2.5. Spectral Modeling

Here we analyze all the spectra given in Figure 4 more quantitatively. In this section, the data from the 12 separate observations are combined only for the purpose of display but left unmerged in the actual spectral analysis. We instead fit 12 individual spectra from the identical sky regions simultaneously, using the response matrices generated independently.
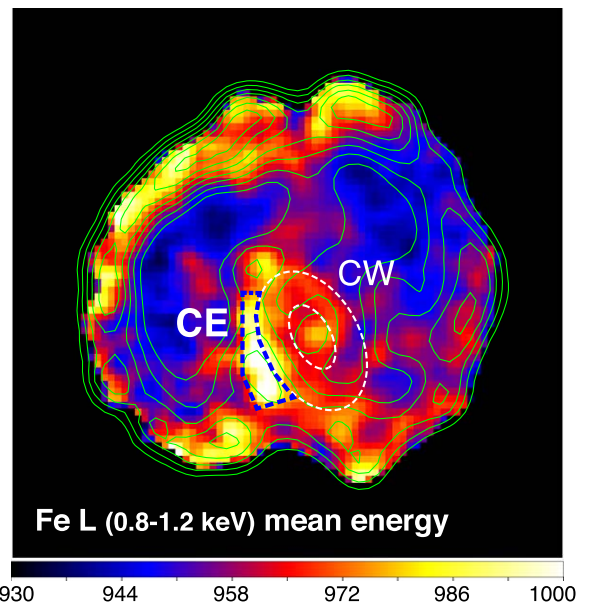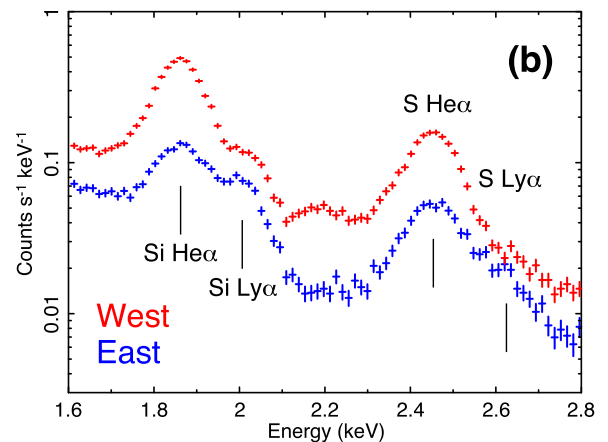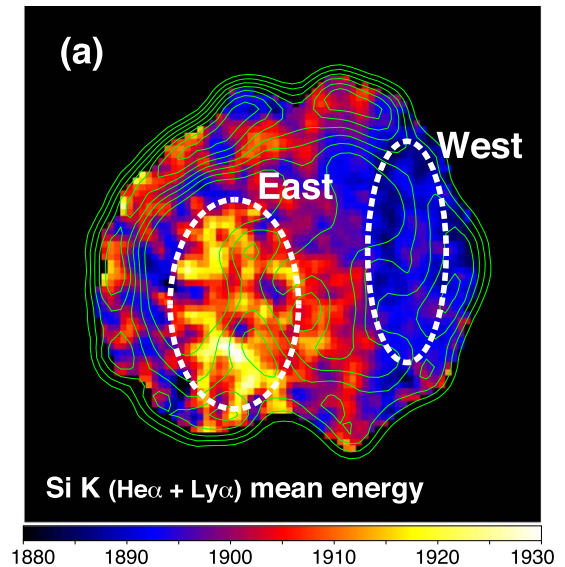
**Table 1**
Best-fit Spectral Parameters

| Component | Parameter | NW | CW | NE | CE |
|---|---|---|---|---|---|
| Absorption | $N_{\rm H}^{\rm LMC}$ ($10^{21}$ cm$^{-2}$) | $3.3 \pm 0.3$ | $3.5 \pm 0.1$ | $6.5^{+1.0}_{-1.1}$ | $2.0^{+0.4}_{-0.7}$ |
| CSM | $kT_{\rm e}$ (keV) | $0.29 \pm 0.01$ | $0.72 \pm 0.01$ | $0.20 \pm 0.01$ | $0.64^{+0.06}_{-0.05}$ |
| | $n_{\rm e}n_{\rm H}V$ ($10^{58}$ cm$^{-3}$) | $5.0^{+0.5}_{-0.6}$ | $4.0 \pm 0.1$ | $2.9^{+1.5}_{-1.1}$ | $0.16^{+0.04}_{-0.01}$ |
| Fe ejecta | $kT_{\rm e}$ (keV) | $8.6^{+0.5}_{-0.4}$ | $7.1^{+0.4}_{-0.5}$ | $11^{+4}_{-3}$ | $42 \pm 30$ |
| | $\tau$ ($10^{10}$ cm$^{-3}$ s) | $1.3 \pm 0.1$ | $3.4 \pm 0.1$ | $2.3^{+0.3}_{-0.2}$ | 3.4 (fixed) |
| | $n_{\rm e}n_{\rm Fe}V$ ($10^{53}$ cm$^{-3}$) | $1.4 \pm 0.1$ | $7.1^{+0.5}_{-0.1}$ | $0.68^{+0.13}_{-0.12}$ | $0.26 \pm 0.07$ |
| IME ejecta | $kT_{\rm e}$ (keV) | $1.6 \pm 0.1$ | $1.7 \pm 0.1$ | $2.2 \pm 0.4$ | $1.6^{+0.2}_{-0.1}$ |
| | Mg (solar) | $0.77^{+0.09}_{-0.12}$ | $1.7 \pm 0.1$ | $2.2 \pm 0.4$ | $1.6^{+0.2}_{-0.1}$ |
| | Si (solar) | $3.6^{+0.3}_{-0.4}$ | $6.0^{+0.2}_{-0.4}$ | $9.7^{+1.9}_{-2.0}$ | $4.3^{+0.6}_{-0.5}$ |
| | S (solar) | $3.4 \pm 0.3$ | $7.2^{+0.3}_{-0.5}$ | $9.2^{+1.5}_{-1.6}$ | $4.4 \pm 0.5$ |
| | Ar (solar) | $3.6 \pm 0.6$ | $9.3^{+1.0}_{-0.8}$ | $8.4 \pm 1.6$ | $5.5^{+1.1}_{-0.7}$ |
| | Ca (solar) | $4.5^{+1.2}_{-1.0}$ | $17 \pm 2$ | $17 \pm 3$ | $6.4 \pm 1.4$ |
| | Cr, Mn (solar) | (tied to Ca) | $61^{+14}_{-11}$ | (tied to Ca) | (tied to Ca) |
| | Fe, Ni (solar) | $0.98^{+0.08}_{-0.12}$ | $2.1^{+0.2}_{-0.1}$ | $1.8^{+0.4}_{-0.5}$ | $2.7 \pm 0.3$ |
| | $\tau$ ($10^{10}$ cm$^{-3}$ s) | $7.5^{+0.8}_{-0.5}$ | $26^{+7}_{-4}$ | $9.3^{+3.0}_{-1.9}$ | $37^{+7}_{-10}$ |
| | $v$ (km s$^{-1}$) | $-1400^{+200}_{-100}$ | $95^{+53}_{-47}$ | $-740^{+90}_{-50}$ | $1200 \pm 100$ |
| | $n_{\rm e}n_{\rm H}V$ ($10^{57}$ cm$^{-3}$) | $6.2^{+0.8}_{-0.5}$ | $5.7^{+0.1}_{-0.9}$ | $2.3^{+0.9}_{-0.4}$ | $3.7^{+0.4}_{-0.6}$ |
| c-stat/d.o.f. | | 3956/6126 | 5010/6125 | 3914/6126 | 3744/6127 |
| Major component | | CSM | Fe ejecta | IME ejecta | IME ejecta |

**Note.** The abundances are relative to the solar values of Wilms et al. (2000). The negative values of the radial velocity ($v$) indicate blueshift.

Since our GMCA method has identified the physical components likely associated with CSM, Fe ejecta, and IME ejecta, we initiate spectral modeling with three components of absorbed thermal plasmas with different compositions. The free parameters are listed in Table 1. For the foreground extinction, we consider both Galactic and Magellanic absorption columns by introducing a TBabs model with the solar abundance (Wilms et al. 2000) and a TBvarabs model with the LMC abundance (Dopita et al. 2019). The hydrogen column density $N_{\rm H}$ of the former is fixed at $6 \times 10^{20}$ cm$^{-2}$ (Dickey & Lockman 1990), whereas that of the latter is left as a free parameter. For the CSM component, we introduce a vapec model (Foster et al. 2012) with the elemental abundances fixed at the LMC mean values, assuming a collisional ionization equilibrium (CIE) for this plasma. Since the previous work suggested nonequilibrium ionization (NEI) for the plasma corresponding to this component (van der Heyden et al. 2002; Lewis et al. 2003), we also try to apply a vnei model alternatively. However, the ionization parameter $\tau = \int n_{\rm e} \, dt$ is always obtained to be $\gtrsim 10^{12}$ cm$^{-3}$ s (in all the four regions), consistent with the CIE. For the Fe ejecta component, we assume a pure-metal plasma in the NEI condition, with no admixture of elements other than Fe and Ni.[7] The abundance ratio between these two elements is assumed to be the solar value of Wilms et al. (2000). Since no hydrogen is contained in this component, its emission measure is defined as a product of the electron and Fe densities and the emitting volume, $n_{\rm e}n_{\rm Fe}V$, instead of $n_{\rm e}n_{\rm H}V$. Lastly, another NEI model is applied to the IME ejecta component, where abundances of the elements not listed in Table 1 are all set to zero. The parameter $v$, the line-of-sight velocity, is allowed to vary to reproduce a small red- or blueshift detected in the IME emission. The spectral fitting is

performed based on the $C$-statistic (Cash 1979) on unbinned spectra using the XSPEC software version 12.10.0 c.

The model described above gives a good fit to the spectrum of each region in the 0.5–8.0 keV band, except for the energies around 1.25 keV. The discrepancy between the data and model found around this energy is likely due to the incompleteness of the atomic data (e.g., inaccurate emissivity of high-level L-shell transitions of Fe and/or Ni). We thus add a single Gaussian to compensate for this incompleteness. The best fit is then obtained as given in Figure 7 and Table 1. The results confirm the validity of our identification of the three components (Section 2.2): the soft X-rays that dominate the O K emission are well reproduced by the low-$kT_{\rm e}$ plasma with the LMC mean abundances. The Fe K-shell emission and a part of the L-shell emission are successfully modeled with a pure-metal Fe-rich plasma. The emission from the IME requires another component with significantly enhanced abundances of these elements with respect to the LMC mean values. We also confirm that the ionization parameter ($\tau$) of the IME ejecta is highest at the CE region and lowest at the NW region, as inferred from Figure 6(a). This result is in contrast to the previous work by Lewis et al. (2003), where little spatial variation in the ionization parameter was found for the IME component. Lewis et al. (2003) also claimed that the IME ejecta component was virtually in the CIE. Our results, on the other hand, indicate evidence for the NEI ($\tau \lesssim 10^{11}$ cm$^{-3}$ s). This discrepancy arises likely because the previous work used data from the early Chandra observations with much shorter exposure, and their spectral analysis focused solely on the radial trend assuming no azimuthal variation in the plasma properties.

The ionization parameter of the Fe ejecta is found to be significantly lower than that of the IME ejecta in any regions (Table 1). This is a common characteristic of SNRs Ia (e.g., Badenes et al. 2007; Sawada et al. 2019; Fukushima et al. 2020) and indicates the stratified elemental composition with

---

[7] A model based on this assumption is often applied to Fe ejecta in SNRs Ia, such as Tycho SNR (Yamaguchi et al. 2017).
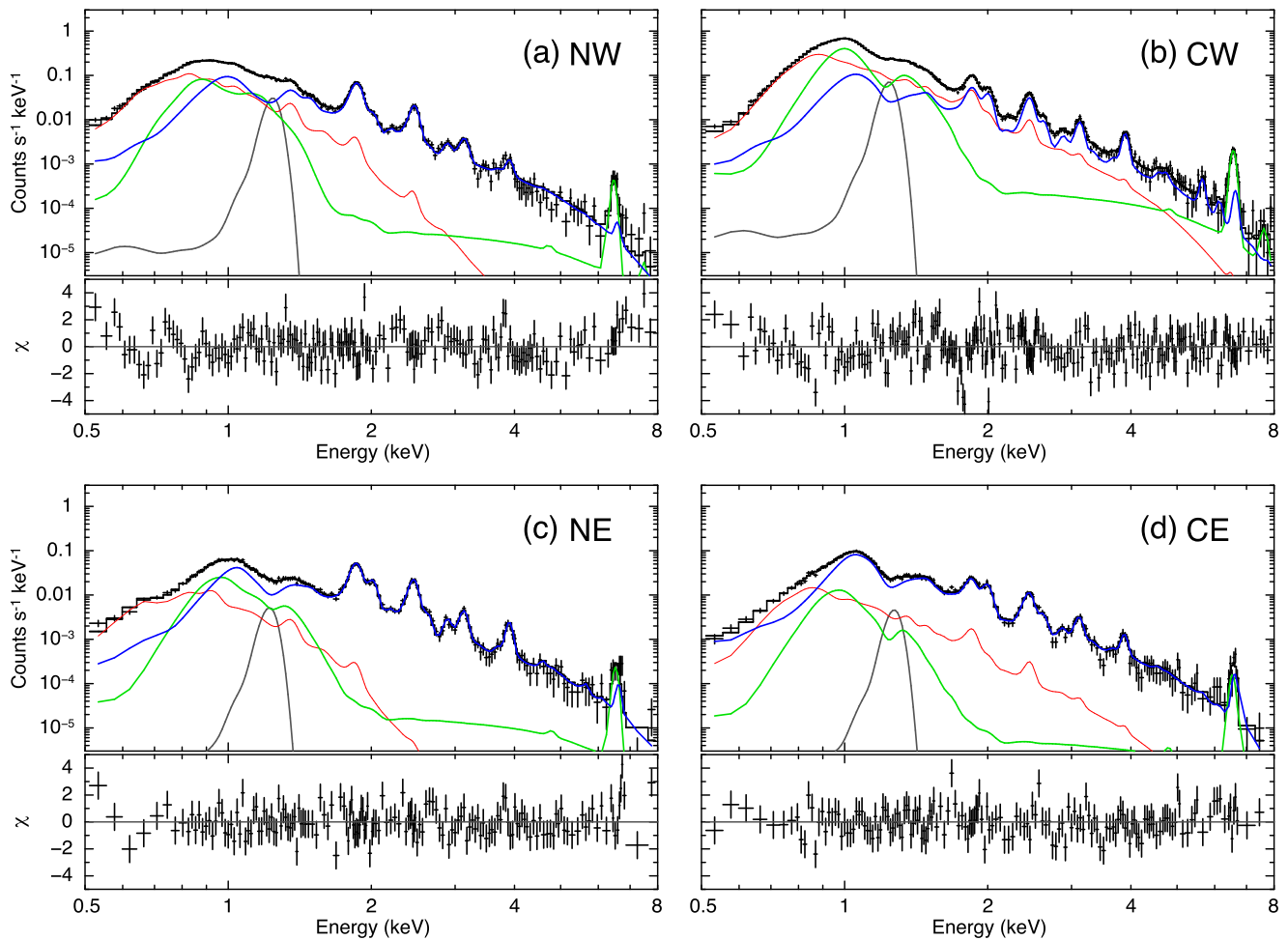
**Figure 7.** ACIS spectra of (a) NW, (b) CW, (c) NE, and (d) CE. The best-fit models for the CSM, Fe ejecta, and IME ejecta components are given as red (thin), green, and blue lines, respectively. The gray curve is an additional Gaussian component to compensate for incompleteness of the atomic data. Spectra from different observations are merged and binned only for the purpose of display.

Fe at the interior so that the Fe ejecta are heated by the reverse shock more recently than the IME ejecta. Such elemental stratification is indeed observed in the radial profile shown in Figure 2.

We detect relatively strong Cr K emission at ~5.6 keV in the CW spectrum, which requires a high Cr abundance of the IME ejecta component ($61^{+14}_{-11}$ solar). Given that the CW region is dominated by the Fe ejecta component rather than the IME ejecta, the Cr in this region could be associated with the former. In fact, the spectrum can also be well reproduced if we fit the Cr abundance of the Fe ejecta component, instead of the assumption in our baseline model (Table 1). In this case, the Cr/Fe abundance ratio is obtained to be ~3.6 solar.

The absorption column density of the NE region is found to be about twice higher than that of the other regions. We note, however, that the currently available data do not allow us to conclude whether this difference is real. Even if we fix the absorption column at $3.0 \times 10^{21}$ cm$^{-2}$, a good fit is obtained with a c-stat/d.o.f. value of 3923/6127, a slightly higher $kT_e$ for the CSM component ($0.23 \pm 0.01$ keV), and a lower Mg abundance for the IME ejecta component ($0.60^{+0.25}_{-0.08}$ solar). The other spectral parameters do not change significantly from the best-fit values in Table 1.
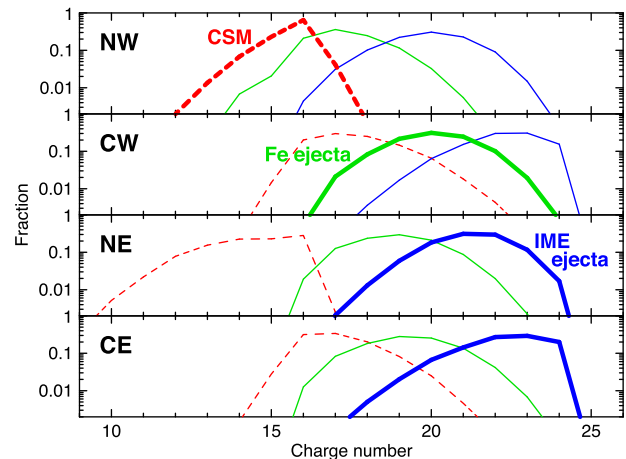


**Figure 8.** Charge distribution of Fe ions in each component in each region. Red (dashed), green, and blue are the CSM, Fe ejecta, and IME ejecta components, respectively. The bold lines represent the dominant component in the spectra as reported in Table 1.

### 2.6. Charge Balance

In Figure 8, we show the charge distributions of Fe in each component in each region, calculated using the plasma parameters obtained in Table 1. We confirm that Fe ions in
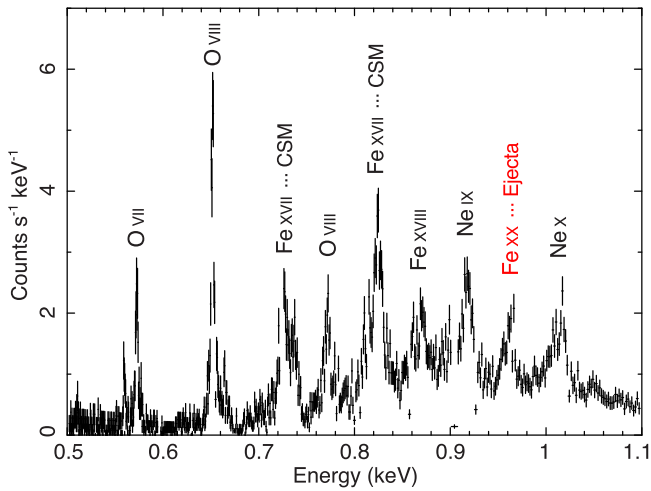
**Figure 9.** RGS1 first-order spectrum of N103B in 0.5–1.1 keV, extracted from the archival XMM-Newton data of ObsID = 0113000301.

the IME component are more highly ionized than in the others, as inferred from the spatial correlation between the mean energy of the Fe L emission and the fraction of the IME component (Figure 5).

Figure 8 also indicates the difference in the Fe charge population between the CSM and Fe ejecta components; the former is dominated by $Fe^{16+}$ and $Fe^{17+}$, whereas the latter by $Fe^{19+}$ and $Fe^{20+}$. Notably, this result explains why N103B was once misinterpreted as a core-collapse SNR by the XMM-Newton/RGS study (van der Heyden et al. 2002). To help the following discussion, we show in Figure 9 the first-order RGS spectrum of the whole SNR obtained from the archival XMM-Newton data of ObsID = 0113000301, which exhibits the strong O VII and O VIII emission as well as the Fe XVII emission. In the previous work, it was assumed that those emission lines originate from the SN ejecta, and the near-solar Fe/O abundance ratio was obtained. This result led to the core-collapse interpretation, since SN Ia nucleosynthesis models generally predict much higher Fe/O ratios. However, the O emission from this SNR is now known to be associated with the CSM (e.g., Williams et al. 2014; Li et al. 2017; Ghavamian et al. 2017, and this work), and our analysis indicates that the Fe XX emission is also dominated by the the CSM component. We can therefore conclude that the previous measurement simply represents the elemental composition of the CSM, and is not in contradiction to the SN Ia classification.

It is also worth noting that the Fe XX L-shell emission is detected in the RGS spectrum at ∼0.96 keV, which likely originates from the Fe ejecta according to our analysis. This inference is further supported if a spatial correlation between this emission and the Fe K emission is revealed. Figure 10(a) shows a zeroth-order image from the archival data of Chandra High-Energy Transmission Grating (HETG) observations of N103B (ObsID = 1045), where the dispersion direction of the Medium Energy Grating (MEG) is indicated with the green lines. The regions A and B correspond to where the CSM and Fe ejecta components are dominant, respectively. Figure 10(b) shows negative first-order spectra of the MEG from the regions A (black) and B (red), confirming that the Fe XX emission at ∼0.96 keV is indeed prominent in the latter (i.e., Fe ejecta). Unfortunately, dispersive spectrometers like the RGS and HETG are not up to further detailed spatially resolved spectroscopy of extended sources. Future microcalorimeter
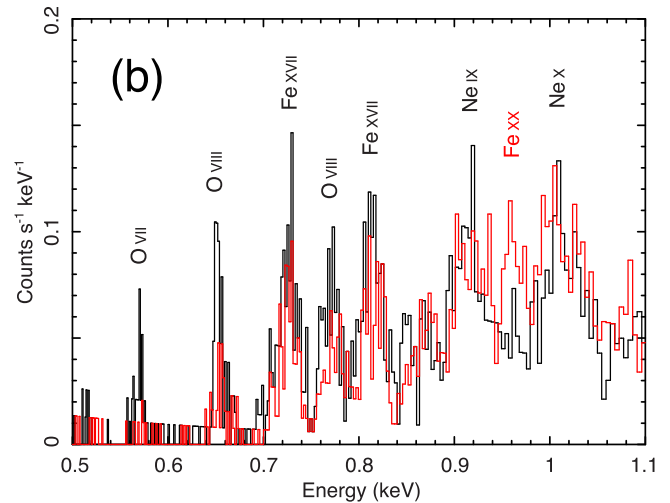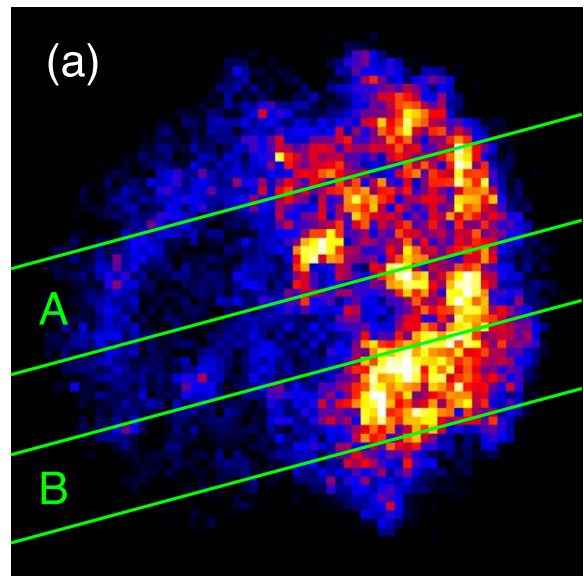




**Figure 10.** (a) Zeroth-order image of N103B from the archival data of the Chandra HETG observations of ObsID = 1045. The green lines indicate the dispersion direction of the MEG as well as where the spectra of the CSM dominant region (A) and the Fe ejecta dominant region (B) are extracted. (b) Negative first-order MEG spectra of the regions A (black) and B (red). The emission at ∼0.96 keV is prominent only in the latter.

observations with sufficient spatial resolution, which will be enabled by the Athena X-ray Integral Field Unit (X-IFU: Barret et al. 2018), are necessary for better identification of the major origin of each individual emission line. We also emphasize that, in principle, our component separation method (GMCA) could work even better for high spectral resolution data cubes as the spectral diversity of physical components would be enhanced.

## 3. Interpretation and Discussion

In this work, we have applied the GMCA technique (Bobin et al. 2016; Picquenot et al. 2019) to the deep Chandra observations of N103B, discovering the double-ring structure of the IME ejecta as well as the more spatially confined Fe-rich ejecta of this SNR. The ionization degree of the IME ejecta is highest in the CE region that corresponds to the east edge of the west ring. This indicates that the CE region is the geometrical outermost of the SNR, although located near the projected SNR
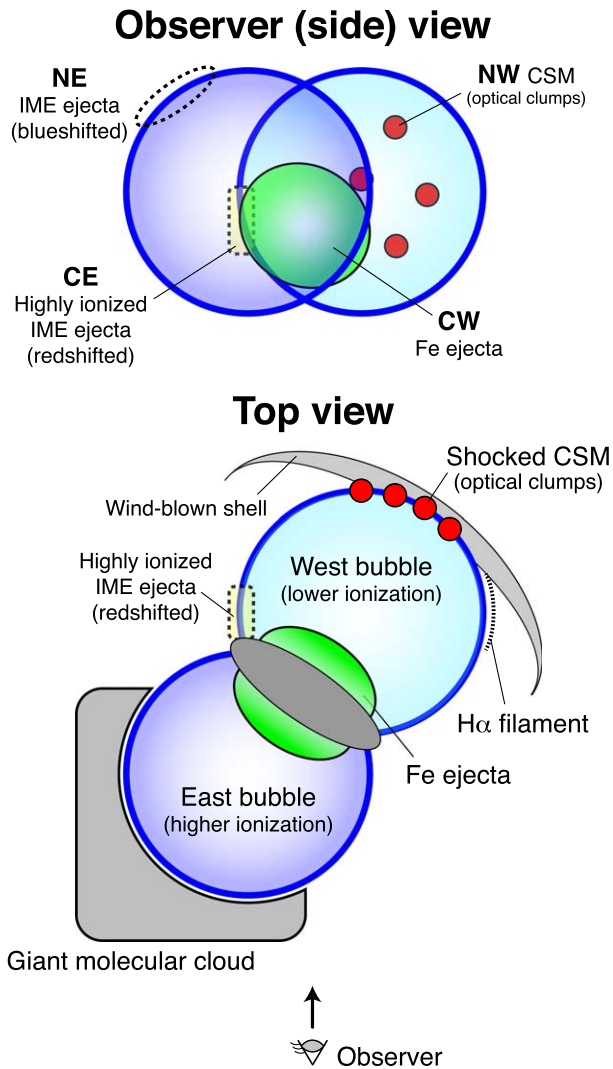
## Observer (side) view



**Figure 11.** Schematic view of the interpreted geometry of the SNR N103B and its environment.

center. The spatial distribution of the IME ionization state (represented by the Si $Ly\alpha/He\alpha$ ratio) shows a clear bimodality, high/low in the East/West bubbles, suggesting that the two bubbles are spatially isolated from each other. We also find that the IME ejecta in the NE/CE regions (both located at the geometrical outermost) are significantly blue/redshifted with respect to the local LMC ISM ($v \sim 260$ km s$^{-1}$). Although these measurements are subject to the uncertainties in gain calibrations, the observed velocities may represent the bulk motion of the outermost ejecta.

As a coherent interpretation of these observational results and the previous multiwavelength studies of this SNR, we propose that N103B forms a bipolar structure, similarly to SN 1987A and typical planetary nebulae (e.g., NGC 2346), and is seen as a double-ring shape by the projection. A schematic of our interpretation is shown in Figure 11. We assume that a dense CSM disk or torus (gray ellipse in the figure) had been formed around the progenitor prior to the SN explosion, causing a faster expansion of the SN ejecta toward the polar directions to form the bipolar bubbles. A similar geometry is suggested for Kepler's SNR, where a substantial amount of CSM is found around the projected SNR center (in addition to the more prominent northern rim), leading to an interpretation

of disk distribution of the CSM at the equatorial plane of the progenitor binary system (Burkey et al. 2013; Chiotellis et al. 2020). An important difference between the two objects is that the system is viewed at an angle of $\sim 45°$ in N103B compared to nearly edge-on in Kepler's SNR, so the bipolar shells of N103B are partially overlapping with each other on the projected sky.

The X-ray surface brightness of N103B is $\sim 5$ times higher in the west than in the east, indicating that the current plasma density is about twice higher in the west (since the X-ray flux is proportional to $n_e^2$). In contrast, the ionization degree of the IME ejecta, which depends on $\int n_e\,dt$, is substantially higher in the east. This apparent discrepancy implies a complex density gradient in the pre-explosion ambient medium. The density immediately around the progenitor must have been higher toward the east, so the IMEs ejected to this direction got highly ionized shortly after the SN explosion. On the other hand, the west bubble must have expanded in a lower-density cavity during the early SNR evolution, and have recently reached a dense wind-blown shell.

Figure 12(a) shows an $H\alpha$ image of N103B obtained by the Wide Field Camera 3 (WFC3) aboard the HST (Li et al. 2017). The faint filaments found in the western half represent collisionless forward shocks propagating into the mostly neutral ambient medium in the cavity. The $H\alpha$ image also exhibits dense radiative clumps inside the Balmer-dominated filamentary shell, which coincide with the CSM component identified in X-rays (the green contours in Figure 12(a)). The $H\alpha$ emission from these clumps is significantly redshifted with respect to the local background and filamentary shell (Li et al. 2017; Ghavamian et al. 2017), suggesting that the clumps are physically located at the backside of the west bubble, where the SNR forward shock is interacting with the wind-blown shell. The total mass of the optical clumps is estimated to be 0.1–3 $M_\odot$ (Williams et al. 2014; Li et al. 2017; Blair et al. 2020). Figure 12(b) presents the radial velocity of the $H\alpha$ clumps measured using the Multi Unit Spectroscopic Explorer (MUSE) on the Very Large Telescope. Details of the observations and data reduction will be presented in a separate paper (C.-J. Li et al. 2021 in preparation). We reveal that the highest radial velocity is achieved at the middle of the west bubble (indicated as the magenta arrow in Figure 12(b)). This result supports our bipolar shell scenario; if the SNR is spherically symmetric with respect to the geometric center of the X-ray emission, a higher radial velocity should be achieved further east.

Interestingly, the eastern half of the SNR shell is completely missing in the $H\alpha$ image. To interpret the lack of this emission, previous optical/infrared studies suggested that the progenitor binary system had a high proper motion toward the west, creating an asymmetric distribution of the CSM (Li et al. 2017; Williams et al. 2014). This interpretation is analogous to Kepler's SNR, where the north–south contrast of the CSM density is indeed caused by the proper motion of the progenitor (Blair et al. 2007; Chiotellis et al. 2012; Williams et al. 2012; Burkey et al. 2013). However, recent radio observations with the ATCA and ALMA discovered a giant molecular cloud interacting with the southeast rim of the SNR (Sano et al. 2018), whose average density ($n_{H_2} \sim 1500\,\text{cm}^{-3}$) is even higher than that of the $H\alpha$ clumps ($n_H \sim 500\,\text{cm}^{-3}$). This suggests that the asymmetry of the $H\alpha$ emission is owing to the difference in the phase of hydrogen rather than the density
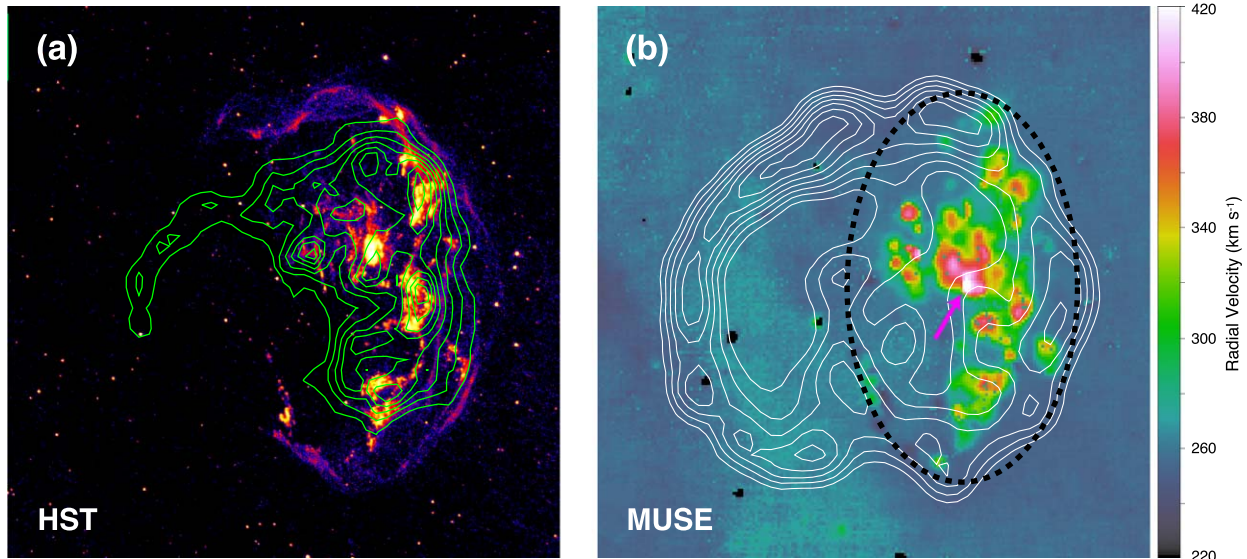
**Figure 12.** (a) Hα image of the SNR N103B with the HST/WFC3, overplotted with the contours of the CSM component (the same as Figure 1(b)). Both are well correlated with each other. (b) Radial velocity of the Hα clumps measured with the MUSE observation, overplotted with the contours of the IME ejecta (the same as Figure 3(b)). The local ISM velocity (∼260 km s⁻¹) is not subtracted. The highest velocity is observed at the region pointed out by the magenta arrow. The black ellipse indicates the rough position of the Hα filaments, which corresponds to the "west bubble." The identical sky region is presented in both panels.

contrast; the ambient medium to the east is dominated by molecules and thus hardly emits the Balmer lines.

Unlike the case of Kepler's SNR, we have not yet conclusively identified emission from the central CSM torus. We note, however, that the projection makes it difficult to spatially resolve the torus (if any) from the backside CSM in the bright western half. Figure 1(e) shows that the relatively faint emission from the shocked CSM is present in the eastern half of the SNR. Moreover, the brightness profile of this component peaks at a smaller radius than those of the IME and Fe ejecta (Figure 2). If this component is associated with the central CSM torus, a redshift of ∼1.1 ($v$/500 km s⁻¹) eV is expected for the O VIII lines, which can only be detected by high-resolution spectrometers with adequate angular resolution, such as the Athena X-IFU.

A torus-like CSM as well as bipolar cavities are often observed in planetary nebulae. In the case of N103B, however, the companion is suggested to be a main-sequence star from the abundance study (Blair et al. 2020), which rules out a planetary nebula origin, or the so-called core-degenerate scenario (e.g., Kashi & Soker 2011; Tsebrenko & Soker 2015; Chiotellis et al. 2020). In the context of the SD scenario, it is theoretically predicted that optically thick winds from the progenitor WD are driven by the mass accretion from the main-sequence companion (Hachisu et al. 1996). When the winds are strong enough, they collide with the companion and strip off its surface layer (Hachisu & Kato 2003a, 2003b). The stripped-off materials then form a massive (a few $M_\odot$) circumstellar torus on the orbital plane (Hachisu et al. 2008), which leads to the formation of hourglass-like cavities toward the polar direction by the fast wind from the WD. Notably, this scenario suggests a relatively short delay time of ∼100 Myr (i.e., the age of the progenitor system at the SN Ia explosion), consistent with the estimate from the star formation history in the SNR site (Badenes et al. 2009). The efficient optically thick wind requires high metallicity (e.g., Kato & Hachisu 1994), which is also consistent with another observational constraint for N103B (≳1 $Z_\odot$: Martínez-Rodríguez et al. 2017).

Interaction between SN ejecta and torus-like CSM was suggested for SN 2012dn, a candidate of the bright, super-Chandrasekhar SN Ia (Yamanaka et al. 2016; Nagao et al. 2018). Kepler's SNR is also thought to originate from a luminous SN Ia (Patnaude et al. 2012; Katsuda et al. 2015). While the peak luminosity of the supernova N103B has not been robustly determined due to the lack of published light echo spectroscopy, the presence of the strong Fe Kα emission implies its luminous SN Ia origin (Yamaguchi et al. 2014; Martínez-Rodríguez et al. 2018). An association between SD progenitors and luminous SNe Ia is therefore suggested, in line with some theoretical predictions (e.g., Fisher & Jumper 2015).

## 4. Conclusions

We have presented an X-ray study of N103B, a young SNR Ia that is known to be interacting with the dense ambient medium. Applying our novel GMCA method to the deep (∼400 ks) Chandra observations, we have discovered the double-ring structure of the IME ejecta. Our detailed spectroscopic study has allowed us to obtain a better understanding of the three-dimensional geometry of the SNR. The preferred scenario is that the pre-explosion stellar winds from the progenitor system had created a dense CSM torus and an hourglass-shape cavity, in which the SNR is expanding to form the bipolar shells. This scenario strongly favors an SD progenitor as the origin of this SNR, consistent with the previous multiwavelength study (e.g., Williams et al. 2014; Li et al. 2017; Sano et al. 2018).

There are several open issues left for our future work. First, it is crucial to identify X-ray emission from the central CSM torus to provide conclusive evidence of our bipolar geometry scenario. Although we have argued that the relatively faint CSM component extended to the east (see Figure 1(e)) could be associated with the central torus, measurement of its radial velocity is necessary to conclude if this is indeed the case. Such a study requires spatially resolved high-resolution spectroscopy that will be enabled by the Athena X-IFU. Second, although it has not been the main focus of the present work, our GMCA

has determined the detailed morphology of the Fe ejecta as well, revealing an intriguing ring structure around the SNR center (Figure 1(c)). Further investigation is required to determine if this structure is formed due to the SN explosion itself or interaction with the ambient medium.

### ORCID iDs

Hiroya Yamaguchi https://orcid.org/0000-0002-5092-6085
Fabio Acero https://orcid.org/0000-0002-6606-2816
Chuan-Jui Li https://orcid.org/0000-0003-1449-7284
You-Hua Chu https://orcid.org/0000-0003-3667-574X

### References

Alsaberi, R. Z. E., Barnes, L. A., Filipović, M. D., et al. 2019, Ap&SS, 364, 204
Badenes, C., Harris, J., Zaritsky, D., & Prieto, J. L. 2009, ApJ, 700, 727
Badenes, C., Hughes, J. P., Bravo, E., & Langer, N. 2007, ApJ, 662, 472
Barret, D., Lam Trong, T., den Herder, J.-W., et al. 2018, Proc. SPIE, 10699, 106991G
Blair, W. P., Ghavamian, P., Long, K. S., et al. 2007, ApJ, 662, 998
Blair, W. P., Ghavamian, P., Raymond, J. C., et al. 2020, ApJ, 902, 153
Blair, W. P., Long, K. S., & Vancura, O. 1991, ApJ, 366, 484
Bobin, J., Sureau, F., & Starck, J. L. 2016, A&A, 591, A50
Borkowski, K. J., Blondin, J. M., & Sarazin, C. L. 1992, ApJ, 400, 222
Brown, P. J., Dawson, K. S., de Pasquale, M., et al. 2012, ApJ, 753, 22
Burkey, M. T., Reynolds, S. P., Borkowski, K. J., & Blondin, J. M. 2013, ApJ, 764, 63
Cash, W. 1979, ApJ, 228, 939
Chiotellis, A., Boumis, P., & Spetsieri, Z. T. 2020, Galax, 8, 38
Chiotellis, A., Schure, K. M., & Vink, J. 2012, A&A, 537, A139
Chu, Y.-H., & Kennicutt, R. C, Jr. 1988, AJ, 96, 1874
Dickey, J. M., & Lockman, F. J. 1990, ARA&A, 28, 215
Dimitriadis, G., Rojas-Bravo, C., Kilpatrick, C. D., et al. 2019, ApJL, 870, L14
Dopita, M. A., Seitenzahl, I. R., Sutherland, R. S., et al. 2019, AJ, 157, 50
Fink, M., Röpke, F. K., Hillebrandt, W., et al. 2010, A&A, 514, A53
Fisher, R., & Jumper, K. 2015, ApJ, 805, 150
Foster, A. R., Ji, L., Smith, R. K., & Brickhouse, N. S. 2012, ApJ, 756, 128
Fukushima, K., Yamaguchi, H., Slane, P. O., et al. 2020, ApJ, 897, 62
Gerardy, C. L., & Fesen, R. A. 2001, AJ, 121, 2781
Ghavamian, P., Seitenzahl, I. R., Vogt, F. P. A., et al. 2017, ApJ, 847, 122
Hachisu, I., & Kato, M. 2003a, ApJ, 598, 527
Hachisu, I., & Kato, M. 2003b, ApJ, 590, 445
Hachisu, I., Kato, M., & Nomoto, K. 1996, ApJL, 470, L97
Hachisu, I., Kato, M., & Nomoto, K. 2008, ApJ, 679, 1390
Hamuy, M., Phillips, M. M., Suntzeff, N. B., et al. 2003, Natur, 424, 651
Hitomi Collaboration, Aharonian, F., Akamatsu, H., et al. 2017, Natur, 551, 478
Hughes, J. P., Hayashi, I., Helfand, D., et al. 1995, ApJL, 444, L81
Iben, I., Jr., & Tutukov, A. V. 1984, ApJS, 54, 335
Kashi, A., & Soker, N. 2011, MNRAS, 417, 1466
Kato, M., & Hachisu, I. 1994, ApJ, 437, 802
Katsuda, S., Mori, K., Maeda, K., et al. 2015, ApJ, 808, 49
Kerzendorf, W. E., Strampelli, G., Shen, K. J., et al. 2018, MNRAS, 479, 192
Kerzendorf, W. E., Yong, D., Schmidt, B. P., et al. 2013, ApJ, 774, 99
Kobayashi, C., Leung, S.-C., & Nomoto, K. 2020, ApJ, 895, 138
Lewis, K. T., Burrows, D. N., Hughes, J. P., et al. 2003, ApJ, 582, 770
Li, C.-J., Chu, Y.-H., Gruendl, R. A., et al. 2017, ApJ, 836, 85
Li, C.-J., Kerzendorf, W. E., Chu, Y.-H., et al. 2019, ApJ, 886, 99
Lundqvist, P., Nyholm, A., Taddia, F., et al. 2015, A&A, 577, A39
Maoz, D., Sharon, K., & Gal-Yam, A. 2010, ApJ, 722, 1879
Martínez-Rodríguez, H., Badenes, C., Lee, S.-H., et al. 2018, ApJ, 865, 151
Martínez-Rodríguez, H., Badenes, C., Yamaguchi, H., et al. 2017, ApJ, 843, 35
Nagao, T., Maeda, K., & Yamanaka, M. 2018, MNRAS, 476, 4806
Nomoto, K. 1982, ApJ, 253, 798
Olling, R. P., Mushotzky, R., Shaya, E. J., et al. 2015, Natur, 521, 332
Patnaude, D. J., Badenes, C., Park, S., & Laming, J. M. 2012, ApJ, 756, 6
Picquenot, A., Acero, F., Bobin, J., et al. 2019, A&A, 627, A139
Rest, A., Suntzeff, N. B., Olsen, K., et al. 2005, Natur, 438, 1132
Reynolds, S. P., Borkowski, K. J., Hwang, U., et al. 2007, ApJL, 668, L135
Ruiz-Lapuente, P., Damiani, F., Bedin, L., et al. 2018, ApJ, 862, 124
Sand, D. J., Graham, M. L., Botyánszki, J., et al. 2018, ApJ, 863, 24
Sano, H., Yamane, Y., Tokuda, K., et al. 2018, ApJ, 867, 7
Sawada, M., Tachibana, K., Uchida, H., et al. 2019, PASJ, 71, 61
Schaefer, B. E., & Pagnotta, A. 2012, Natur, 481, 164
Seitenzahl, I. R., Cescutti, G., Röpke, F. K., Ruiter, A. J., & Pakmor, R. 2013, A&A, 559, L5
Shappee, B. J., Stanek, K. Z., Pogge, R. W., & Garnavich, P. M. 2013, ApJL, 762, L5
Shen, K. J., Kasen, D., Miles, B. J., & Townsley, D. M. 2018, ApJ, 854, 52
Silverman, J. M., Nugent, P. E., Gal-Yam, A., et al. 2013, ApJS, 207, 3
Simon, J. D., Gal-Yam, A., Gnat, O., et al. 2009, ApJ, 702, 1157
Sternberg, A., Gal-Yam, A., Simon, J. D., et al. 2011, Sci, 333, 856
Suzuki, N., Rubin, D., Lidman, C., et al. 2012, ApJ, 746, 85
Totani, T., Morokuma, T., Oda, T., Doi, M., & Yasuda, N. 2008, PASJ, 60, 1327
Tsebrenko, D., & Soker, N. 2015, MNRAS, 453, 166
Tucker, M. A., Shappee, B. J., & Wisniewski, J. P. 2019, ApJL, 872, L22
van der Heyden, K. J., Behar, E., Vink, J., et al. 2002, A&A, 392, 955
Webbink, R. F. 1984, ApJ, 277, 355
Whelan, J., & Iben, I., Jr. 1973, ApJ, 186, 1007
Williams, B. J., Blair, W. P., Borkowski, K. J., et al. 2018, ApJL, 865, L13
Williams, B. J., Borkowski, K. J., Reynolds, S. P., et al. 2012, ApJ, 755, 3
Williams, B. J., Borkowski, K. J., Reynolds, S. P., et al. 2014, ApJ, 790, 139
Williams, R. M., Chu, Y.-H., Dickel, J. R., et al. 1999, ApJS, 123, 467
Wilms, J., Allen, A., & McCray, R. 2000, ApJ, 542, 914
Yamaguchi, H., Badenes, C., Petre, R., et al. 2014, ApJL, 785, L27
Yamaguchi, H., Hughes, J. P., Badenes, C., et al. 2017, ApJ, 834, 124
Yamanaka, M., Maeda, K., Tanaka, M., et al. 2016, PASJ, 68, 68